2019

Enhanced superconductivity induced by several-unit-cells diffusion in an FeTe/FeSe bilayer heterostructure

Wenbin Qiu
University of Wollongong, wq118@uowmail.edu.au

Qingshuang Ma
Tianjin University

Zongqing Ma
University of Wollongong, zqma@uow.edu.au

Jun Tan
Sichuan University

Lina Sang
University of Wollongong, ls906@uowmail.edu.au

See next page for additional authors

Publication Details

Qiu, W., Ma, Q., Ma, Z., Tan, J., Sang, L., Cai, C., Hossain, M. Al., Cheng, Z., Wang, X., Liu, Y. & Dou, S. Xue. (2019). Enhanced superconductivity induced by several-unit-cells diffusion in an FeTe/FeSe bilayer heterostructure. Physical Review B: Covering condensed matter and materials physics, 99 (6), 064502-1-064502-1.

Enhanced superconductivity induced by several-unit-cells diffusion in an FeTe/FeSe bilayer heterostructure

Abstract

Unlike monolayer Fe-Chalcogenide (Fe-Ch)/SrTiO3 (STO), which possesses the potential for high-temperature superconductivity (HTS), a regular Fe-Ch thin film grown on a non-STO substrate by the pulsed laser deposition method shows totally different superconducting behavior and a different mechanism. Although regular Fe-Ch thick films grown on CaF2 generally show the highest superconducting transition temperature (Tc) compared with any other substrates, the disappearance of superconductivity always takes place when the thickness of the Fe-Ch film is reduced to a critical value (~20nm for Fe-Se and ~30nm for Fe-Se-Te) with the reason still under debate. Here, we report an enhanced Tc≈17.6K in a 7-nm-FeTe/7-nm-FeSe bilayer heterostructure grown on CaF2 substrate. Generally, the Fe-Ch film on CaF2 is supposed to be one order of magnitude greater in thickness to achieve similar performance. Hall measurements manifest the dominant nature of hole-type carriers in the films in this work, which is similar to the case of a pressurized bulk FeSe single crystal, while in sharp contrast to heavily electron-doped HTS Fe-Ch systems. According to the electron energy loss spectroscopy results, we observed direct evidence of nanoscale phase separation in the form of a fluctuation of the Fe-L3/L2 ratio near the FeTe/FeSe interface. In detail, a several-unit-cell-thick Fe(Se,Te) diffusion layer shows a higher Fe-L3/L2 ratio than either an FeTe or an FeSe layer, indicating low Fe 3d electron occupancy, which is, to some extent, consistent with the hole-dominant scenario obtained from the Hall results. It also implies a possible relationship between the state of Fe 3d electron occupancy and the enhanced Tc in this work. Our work clarifies the importance of the FeTe/FeSe interface in reviving the superconductivity in Fe-Ch ultrathin films, contributing to a more unified understanding of unconventional Fe-Ch superconductivity.

Disciplines

Engineering | Physical Sciences and Mathematics

Publication Details

Qiu, W., Ma, Q., Ma, Z., Tan, J., Sang, L., Cai, C., Hossain, M. Al., Cheng, Z., Wang, X., Liu, Y. & Dou, S. Xue. (2019). Enhanced superconductivity induced by several-unit-cells diffusion in an FeTe/FeSe bilayer heterostructure. Physical Review B: Covering condensed matter and materials physics, 99 (6), 064502-1-064502-1.

Authors

Wenbin Qiu, Qingshuang Ma, Zongqing Ma, Jun Tan, Lina Sang, Chuanbing Cai, Md. Shahriar Al Hossain, Zhenxiang Cheng, Xiaolin Wang, Yongchang Liu, and Shi Xue Dou

Enhanced superconductivity induced by several-unit-cells diffusion in an FeTe/FeSe bilayer heterostructure

Wenbin Qiu,[2,3,4] Qingshuang Ma,[1] Zongqing Ma,[1,2,*] Jun Tang,[3] Lina Sang,[2,4] Chuanbing Cai,[4] Mohammed Shahriar Al Hossain,[2] Zhenxiang Cheng,[2] Xiaolin Wang,[2] Yongchang Liu,[1] and Shi Xue Dou[2]

[1]*Tianjin Key Laboratory of Composite and Functional Materials, School of Materials Science & Engineering, Tianjin University, Tianjin 300072, People's Republic of China*

[2]*Institute for Superconducting and Electronic Materials, Australian Institute for Innovative Materials, University of Wollongong, Squires Way, North Wollongong, New South Wales 2500, Australia*

[3]*Key Laboratory of Radiation Physics and Technology of Ministry of Education, Institute of Nuclear Science and Technology, Sichuan University, Chengdu 610064, China*

[4]*Shanghai Key Laboratory of High Temperature Superconductors, Physics Department, Shanghai University, Shanghai 200444, People's Republic of China*

(Received 14 October 2018; revised manuscript received 29 December 2018; published 8 February 2019)

Unlike monolayer Fe-Chalcogenide (Fe-*Ch*)/$SrTiO_3$ (STO), which possesses the potential for high-temperature superconductivity (HTS), a regular Fe-*Ch* thin film grown on a non-STO substrate by the pulsed laser deposition method shows totally different superconducting behavior and a different mechanism. Although regular Fe-*Ch* thick films grown on CaF_2 generally show the highest superconducting transition temperature (T_c) compared with any other substrates, the disappearance of superconductivity always takes place when the thickness of the Fe-*Ch* film is reduced to a critical value (∼20 nm for Fe-Se and ∼30 nm for Fe-Se-Te) with the reason still under debate. Here, we report an enhanced $T_c \approx 17.6$ K in a 7-nm-FeTe/7-nm-FeSe bilayer heterostructure grown on CaF_2 substrate. Generally, the Fe-*Ch* film on CaF_2 is supposed to be one order of magnitude greater in thickness to achieve similar performance. Hall measurements manifest the dominant nature of hole-type carriers in the films in this work, which is similar to the case of a pressurized bulk FeSe single crystal, while in sharp contrast to heavily electron-doped HTS Fe-*Ch* systems. According to the electron energy loss spectroscopy results, we observed direct evidence of nanoscale phase separation in the form of a fluctuation of the Fe-L_3/L_2 ratio near the FeTe/FeSe interface. In detail, a several-unit-cell-thick Fe(Se,Te) diffusion layer shows a higher Fe-L_3/L_2 ratio than either an FeTe or an FeSe layer, indicating low Fe 3*d* electron occupancy, which is, to some extent, consistent with the hole-dominant scenario obtained from the Hall results. It also implies a possible relationship between the state of Fe 3*d* electron occupancy and the enhanced T_c in this work. Our work clarifies the importance of the FeTe/FeSe interface in reviving the superconductivity in Fe-*Ch* ultrathin films, contributing to a more unified understanding of unconventional Fe-*Ch* superconductivity.

DOI: 10.1103/PhysRevB.99.064502

I. INTRODUCTION

Considering that the mechanism of high-temperature superconductivity still remains unsolved [1,2] since its discovery three decades ago [3], scientists are seeking inspiration from novel superconductors, for instance, Fe-based superconductors. Intense debate has been triggered since the survival of superconductivity was found in Fe-based compounds [4] in 2008. Among the numerous types of Fe-based superconductors [4–11], iron selenide [11,12] (FeSe) with the simplest binary structure is an appropriate candidate for investigating the intrinsic mechanism of unconventional superconductivity. Through applying high pressure [13–17], elemental substitution [18–21]/intercalation [22–24], or a liquid-gating technique [25–27], the superconducting transition temperature (T_c) of FeSe crystals can be substantially raised despite the low T_c of ∼8 K [11] in the original bulk FeSe. More surprisingly, the FeSe compound in the form of thin films or multilayers has attracted considerable attention in the past few years due to its potential for achieving significantly high T_c and unique electronic properties.

By employing molecular beam epitaxy [28–37] (MBE), a dramatic enhancement in superconductivity (T_c^{onset} over 40 K/60 K shown by transport/scanning tunnelling spectroscopy measurements) was realized in 1-unit-cell FeSe on a pretreated $SrTiO_3$ (STO) substrate. High-T_c superconductivity (HTS) no longer survives, however, if the film has more than one atomic layer [32,36,37]. The only way to revive superconductivity in a multilayer Fe-Chalcogenide (Fe-*Ch*) thin film is through postengineering for electron doping or enhancing the electron-phonon coupling. For example, an alkali-metal-coating (Li, K) process [38–43] was found promising for introducing massive electron doping into multilayer FeSe films on STO. Wang *et al.* [44] reported that a postannealing procedure is another effective way to introduce electron charge carriers into a multilayer FeSe system and realize an insulator-superconductor transition. A novel method was also proposed

*Corresponding author: mzq0320@163.com

by Shiogai *et al.* [45,46]. They reported their achievements in tuning the thickness and corresponding superconductivity of ultrathin FeSe films on oxide substrates through subtly controlled electrochemical etching and electric-field application. Nevertheless, the STO substrate is a prerequisite in this HTS Fe-*Ch* system, as it transfers massive electron doping into the first Fe-*Ch* unit cell [28,47].

On the other hand, undoped Fe-*Ch* [48–54] thick films grown on a non-STO substrate showed superconducting behavior that is significantly different from the case of monolayer or electron-doped multilayer FeSe. Even though the T_c is currently not comparable with the T_c record achieved in ultrathin FeSe thin films, a deep investigation into the Fe-*Ch* thick film is still of great importance to reveal the universal mechanism behind the superconductivity in Fe-*Ch* and similar systems. Using the pulsed laser deposition (PLD) method, Fe-*Ch* films with T_c^{onset} over 15 K [55] in FeSe, or 21 K [56] in $FeSe_{0.5}Te_{0.5}$, can be easily prepared without external electron doping, although there is a minimum thickness for this system to exhibit superconductivity, empirically over 20 nm for FeSe [53,57,58] and over 30 nm for Fe-Se-Te [43,51,56–60]. Films with less thickness are generally nonsuperconducting or even insulating. Quite a few works have explained the disappearance of superconductivity in ultrathin Fe-*Ch* films. For instance, it is well accepted that severe thermal and quantum fluctuations at low dimensionality usually suppress the T_c of a superconducting film [44]. Tensile stress, which is detrimental to the superconductivity of Fe-Chalcogenide films [59], tends to be induced when the thickness of $FeSe_{0.5}Te_{0.5}$ is lower than 30 nm [56]. Nabeshima *et al.* [53] demonstrated that low T_c in FeSe films thinner than 100 nm was due to the excess-Fe disorder near the surface of the films. The superconducting-insulating transition (SIT) was ascribed to a disorder-driven effect by Schneider *et al.* [55,56] in their FeSe films prepared by a sputtering technique. More recently, we reported similar SIT behavior and ascribed the insulating resistivity behavior of an 8 nm FeSe film to the severely unbalanced FeSe stoichiometry, which is caused by the calcium selenide (CaSe) interlayer that universally exists at $FeSe/CaF_2$ interfaces [55]. Despite the various viewpoints, the intrinsic reason for the suppression of superconductivity in undoped ultrathin Fe-*Ch* films still remains elusive, which is preventing the discovery of HTS in this system. A very recent work published by Kouno *et al.* [60] reported a T_c at 38 K in an $Fe(Se_{0.8}Te_{0.2})$ thin film on CaF_2 substrate. Similar to the top-down approach used by Shiogai [45], they focused on the interface between the $Fe(Se_{0.8}Te_{0.2})$ layer and the ionic liquid electrolyte. Inspired by that, we expected that the upper surface of the Fe-*Ch* thin film would be critical in overcoming the T_c suppression in ultrathin Fe-*Ch* films grown on non-STO substrates.

In this work, we achieved a superconducting transition in an ultrathin 7 nm FeSe film grown on a CaF_2 substrate by simply coating an FeTe capping layer on top. In this bilayer heterostructure, the highest T_c reaches 17.6 K, although superconductivity is generally lacking in ultrathin Fe-*Ch* films grown on non-STO substrates by the PLD method. The enhanced superconductivity is considered to probably result from a several-unit-cell-thick Fe(Se,Te) diffusion layer formed near the FeTe/FeSe interface. Our bilayer films were found to be hole dominated according to Hall measurements, which excludes them from the heavily electron-doped HTS scenario. Localized electron energy loss spectroscopy (EELS) results revealed the abnormal electronic orbital behavior of the interfacial region and hinted at a possible relationship between the low Fe 3*d* electron occupancy and the enhanced superconductivity in Fe-*Ch* thin films. This work is valuable for improving our current understanding of the common suppression of superconductivity in ultrathin Fe-*Ch* films grown on non-STO substrates.

II. EXPERIMENTAL DETAILS

FeSe and FeTe thin films were grown on CaF_2 (100) single-crystal substrates (lattice parameter $a = 5.462$ Å) via PLD [neodymium-doped yttrium aluminium garnet (Nd:YAG) laser, $\lambda = 355$ nm, 10 Hz, 2 W output, ~1.7 nm/ min] under a vacuum better than 4×10^{-6} Torr. First, an FeSe film with a thickness of 7 nm (determined by cross-sectional micrographs) was deposited at a substrate temperature as 300 °C. Afterwards, by directly switching to an FeTe target, the as-grown FeSe film was covered *in situ* by an FeTe layer (same deposition time) with the temperature unchanged. Finally, the bilayer FeTe/FeSe heterostructure (denoted as #FT-300) was naturally cooled down in the evacuated chamber. For comparison, a counterpart (denoted as #FT-r.t.) was separately prepared based on the same procedure for the FeSe layer. The only difference between #FT-300 and #FT-r.t. was that the FeTe layer of the latter was deposited only after the substrate temperature was cooled down to room temperature. Hence, the chemical reaction between the FeSe and FeTe composite was minimized in #FT-r.t. compared with #FT-300. To ensure the identical properties of the as-grown FeSe in two samples, the postannealing effect on the as-grown FeSe in #FT-300 during the FeTe deposition at 300 °C was taken into consideration. A heating process at 300 °C for the same time period was added right after finishing the FeSe deposition in #FT-r.t.

The phase and structure were identified by x-ray diffraction (XRD, GBC MMA) θ-2θ scans with Cu Kα radiation. For microstructure characterizations, an aberration-corrected high-angle annular dark-field—scanning transmission electron microscope (HAADF-STEM, JEOL ARM-200F) equipped with a detector for energy-dispersive x-ray spectroscopy (EDS, Centurio SDD) was employed for acquiring high-resolution micrographs as well as information about elemental distributions from a cross-sectional view. Further STEM-EELS measurements at a spectral resolution of 0.05 eV were performed at room temperature to acquire chemical and bonding information on the specimens. Lamellae for STEM were prepared through the *in situ* lift-out technique in a focused ion-beam (FIB, FEI Helios 600 NanoLab) system. The electrical transport measurements were carried out in a 9 T physical properties measurement system (PPMS, Quantum Design). Commercial gold wires (diameter 25 μm) and conductive silver paint were used in preparing the electrodes for transport resistance measurements.

III. RESULTS AND DISCUSSIONS

Figure 1 shows the transport superconducting performance obtained from the two samples in this work together with the

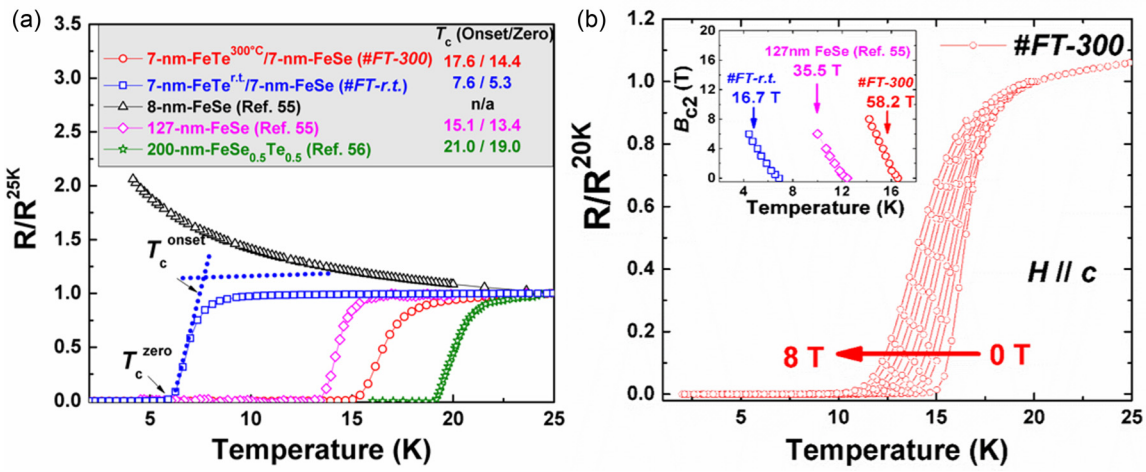

FIG. 1. (a) Temperature dependence of the normalized resistance ($R/R^{25\,K}$) at self-field for #FT-300 and #FT-r.t. in this work from 2 to 25 K. Additionally, the results from a 8 nm FeSe thin film [55] (black triangles), a 127 nm FeSe thin film [55] (magenta diamonds), and a 200 nm $FeSe_{0.5}Te_{0.5}$ thin film [56] (olive stars) are added on the same coordinates for comparison. The T_c^{onset}/T_c^{zero} values for each sample are also given. (b) $R/R^{20\,K}$-T measurements of #FT-300 under external fields up to 8 T along the c axis. The inset shows the plots of B-T_c . The upper critical field (B_{c2}) is estimated from the linear extrapolation of T_c^{mid}. The results from a 127 nm FeSe thin film [55] are also plotted for comparison.

results from Refs. [55,56] for comparison. The temperature dependence of the normalized resistance ($R/R^{25\,K}$) in the low-temperature range (2–25 K) is presented in Fig. 1(a). T_c^{onset} is defined as the crossing point at which the extrapolation from the normal-state resistance intersects with the tangent line of the transition (shown by the dashed lines), while T_c^{zero} refers to the temperature at which the resistance drops to zero. We obtained a $T_c^{onset}/T_c^{zero} = 17.6\,K/14.4\,K$ for #FT-300 and 7.6 K/5.3 K for #FT-r.t. By applying magnetic fields up to 8 T perpendicular to the ab plane of the sample, the ρ-T curves of #FT-300 under external field were plotted, as shown in Fig. 1(b) as an example, and the upper critical field (B_{c2}) was calculated [inset of Fig. 1(b)] depending on the linear extrapolation of the T_c^{mid}, which is defined as the temperature at which the resistivity has dropped to one-half of the value at 25 K. It should be noted that T_c and B_{c2} are both higher in the #FT-300 sample than those from the optimized results obtained in a 127 nm FeSe film in our previous work [55]. Considering that the entire thickness of #FT-300 is no more than 15 nm (including both FeSe and FeTe layers), normally, no superconducting transition would be expected in this sample, which is because traditional FeSe or FeSeTe films with ultrathin thickness always show insulating behavior [55,61], just as in the case of 8 nm FeSe (black triangles) plotted in Fig. 1(a) (excluding the cases of HTS FeSe involving heavy electron doping [28–37,45,46]), and superconductivity is also absent in pure FeTe thin films down to 2 K [62,63]. Thus, the discovery of a superconducting transition in a surprisingly thin FeTe/FeSe bilayer structure is unexpected and definitely worth further exploration to clarify the mechanism. Furthermore, the T_c^{onset} of #FT-300 is 2.5 K higher than the $T_c^{onset} = 15.1\,K$ from a 127 nm FeSe film in our recent work [55] [shown by magenta diamonds in Fig. 1(a)] which is one of the highest T_c's that can be obtained in a pristine PLD-FeSe thin film grown on a CaF_2 substrate. Similar T_c enhancement was also reported in FeSe/FeTe superlattices [52]. FeTe has been widely used as a protective layer on unit-cell FeSe films [28–30,47,64,65]. Although the possibility of Se/Te atom diffusion cannot be excluded, no enhancement in superconductivity was reported after introducing an FeTe layer onto an FeSe film ($T_c \sim 53\,K$ in Si/FeSe/STO from Ref. [28], while $T_c \sim 54.5\,K$ in Si/FeTe/FeSe/STO from Ref. [29]). It was further found by transport measurements that a 14-unit-cell (UC) (~ 8.7 nm) FeTe film was dominated by hole carriers throughout the temperature range from 5 to 300 K [47], which may affect the overall carrier situation of the bilayer structure. There is no distinct change in the Hall resistance results (R_{xy}), however, of 1-UC and 2-UC FeSe films after subtracting the influence of the FeTe layers [65]. Hence, the doping effect on FeSe from the FeTe should be negligible in our case, as the 7 nm FeSe is even thicker than the 2-UC FeSe. The enhanced superconductivity in #FT-300 is probably related to an interface effect between the FeSe and FeTe layers.

Iron-based superconductors always show complex Hall behavior [66–72] due to their multiband nature. We performed Hall measurements for both samples to reach a greater understanding of their transport properties. In order to eliminate the longitudinal resistivity component resulting from the misalignment of electrode contacts, we acquired the transverse resistivity (ρ_{xy}) in both positive and negative fields and then calculated the difference, i.e., $\rho_{xy}(H) = [\rho_{xy}(+H) - \rho_{xy}(-H)]/2$. The final results for the Hall coefficient (R_H) are shown in Fig. 2(a) for #FT-300 and Fig. 2(b) for #FT-r.t. The R_H is determined by the linear fitting of the ρ_{xy} curves between 1 to 4 Tesla so that the contribution from the anomalous Hall effect can be excluded. Herein, the noticeable temperature dependence of R_H provides solid evidence of the multiband nature of the band structure. On cooling down from room temperature, the nearly temperature-independent R_H with positive absolute values above the characteristic temperature $T^* \sim 125\,K$ is considered as proof of a hole-dominated two-band

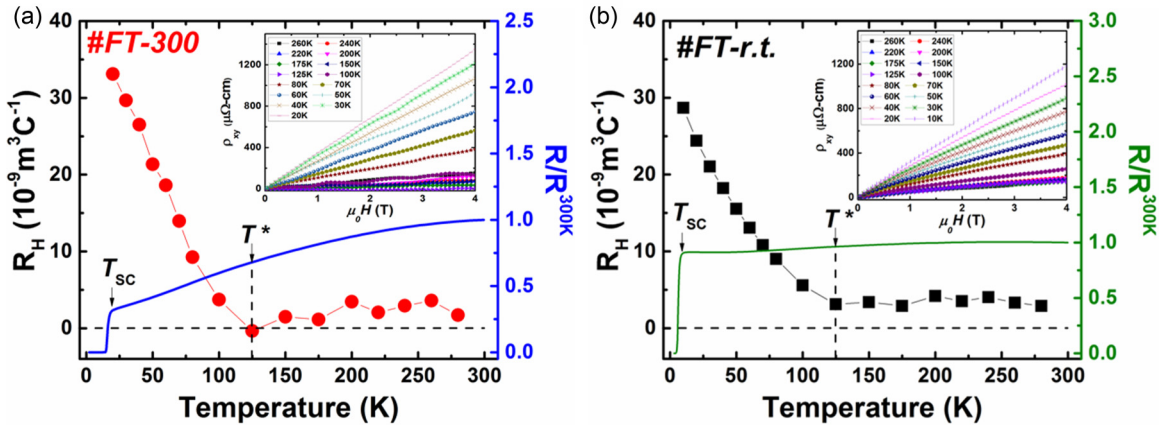

FIG. 2. Temperature dependence of the Hall coefficient R_H (left y axis) and zero-field normalized resistance ($R/R^{300\,K}$) (right y axis) for (a) #FT-300 and (b) #FT-r.t. Insets: Hall resistivity ρ_{xy} vs $\mu_0 H$ at different temperatures.

model. That is to say, the hole pockets around the Γ point in the Fermi surface are governing the transport properties in the high-temperature range. We found that the R_H behavior differs between the two samples near T^*. In #FT-300, R_H changes to a negative small value near T^*, which indicates a predominance of electron-type charge carriers. Below T^*, R_H immediately switches back to positive and exhibits a clear upward deviation. The phenomenon that the sign of R_H changes twice is very similar to that in FeSe flakes without a gate voltage [25] and in an 8-UC FeSe film grown on a STO substrate [47]. It can be interpreted as due to the coexistence of electron- and hole-type carriers with different contributions from various bands [30]. On the contrary, R_H is nearly constant ($\sim 5 \times 10^{-9}$ m^3/C) above T^* in #FT-r.t., indicating an unchanged domination by hole-type carriers. Below T^*, R_H in both samples exhibits a rapid increase on the positive side with decreasing temperature. It reflects the decrease in the electron contribution at low temperature. Similarly, the predominance of hole-type carriers in PLD-grown multilayer FeSe thin films grown on CaF_2 substrates was also verified by angle-resolved photoemission spectroscopy (ARPES) measurements by Shen *et al.* [73]. In other words, the enhanced T_c in #FT-300 could be excluded from the heavily electron-doped HTS scenarios [25,30,44,47,65,66]. In addition, the temperature dependence of the normalized resistance [y axes in Figs. 2(a) and 2(b)] reflects a triple residual resistance ratio (RRR) of #FT-300 than that of #FT-r.t., indicating much better crystallinity quality of #FT-300.

For the determination of phase composition, XRD measurements were carried out, with the results shown in Fig. 3(a) (detection angle, $2\theta = 10$–55°) and Fig. 3(b) ($2\theta = 12$–18°). The spectra are normalized by to the CaF_2 (200) diffraction peak. Overall, both FeTe/FeSe bilayer films in this work have a high-quality c-axis orientation without any indication of macroscopic disorder. The Ag phase in #FT-r.t. has resulted from the residual silver paste on the sample surface after transport measurements. For #FT-r.t., two sets of peaks indexed as FeTe (00l) and FeSe (00l) are shown in the spectrum. The FeTe (00l) peaks are located at lower 2θ angles compared with those of FeSe, which is consistent with the fact that the interplanar distance in the FeTe [74] lattice is larger than that of FeSe [11]. For #FT-300, a similar configuration is also observed, except for the absence of the FeTe (003) peak (due to low intensity). We noticed an additional diffraction peak allocated between FeSe (001) and FeTe (001), suggesting the presence of an isostructural phase with the lattice sitting between FeSe and FeTe. Here, the Fe(Se,Te) phase refers to a diffusion layer between the FeTe and the FeSe, which shows a continuum between the two phases rather than an $FeSe_xTe_{1-x}$ phase with a fixed chemical composition. We are unable to determine the specific composition due to the gradual transition near the FeTe/FeSe interface. The enlarged 2θ range near FeSe (001) is presented in Fig. 3(b) on a logarithmic scale on the y axis. From this viewpoint, an identical FeSe phase is confirmed in #FT-300, and the Fe(Se,Te) (001) peak is clearly distinguished. The FeTe (001) peak in #FT-r.t. is broader, perhaps due to the small amount of Fe(Se,Te) phase unavoidably formed at the FeTe/FeSe interface. Nevertheless, the thickness of the Fe(Se,Te) layer in #FT-r.t. is much lower, so that only a broadened FeTe (001) peak is detected rather than a separate Fe(Se,Te) (001) diffraction peak, as appears in #FT-300. The presence of the Fe(Se,Te) phase is thought to be the determinant that triggers the superconductivity in the sample combined from two nonsuperconducting layers, although why the T_c of #FT-300 is unusually high requires further investigation and will be discussed later in this paper.

After the identification of the crystal structure by XRD from a macroscopic perspective, we confirmed that an Fe(Se,Te) diffusion layer with a lattice parameter located between those of FeSe and FeTe exists in #FT-300, while a only tiny amount of similar phase is present in #FT-r.t. With the help of HAADF-STEM analysis, we can further reveal the local microstructure and determine the morphology of the interface. Figures 3(c) and 3(d) present STEM cross-sectional micrographs focusing on the FeTe/FeSe interface. Along the [010] zone axis, well-aligned tetragonal FeSe films with no more than 10 unit cells are found stacked with a tetragonal FeTe layer. Due to the larger atomic number in Te than in Se, a distinct difference in contrast is observed in both HAADF-STEM images, leading to the brighter appearance of the upper FeTe layer. At a lower magnification (micrographs not shown here), many more disorders (stacking faults, amorphous nanoparticles) are found in #FT-r.t. than in #FT-300 due to the inferior crystallinity of the former,

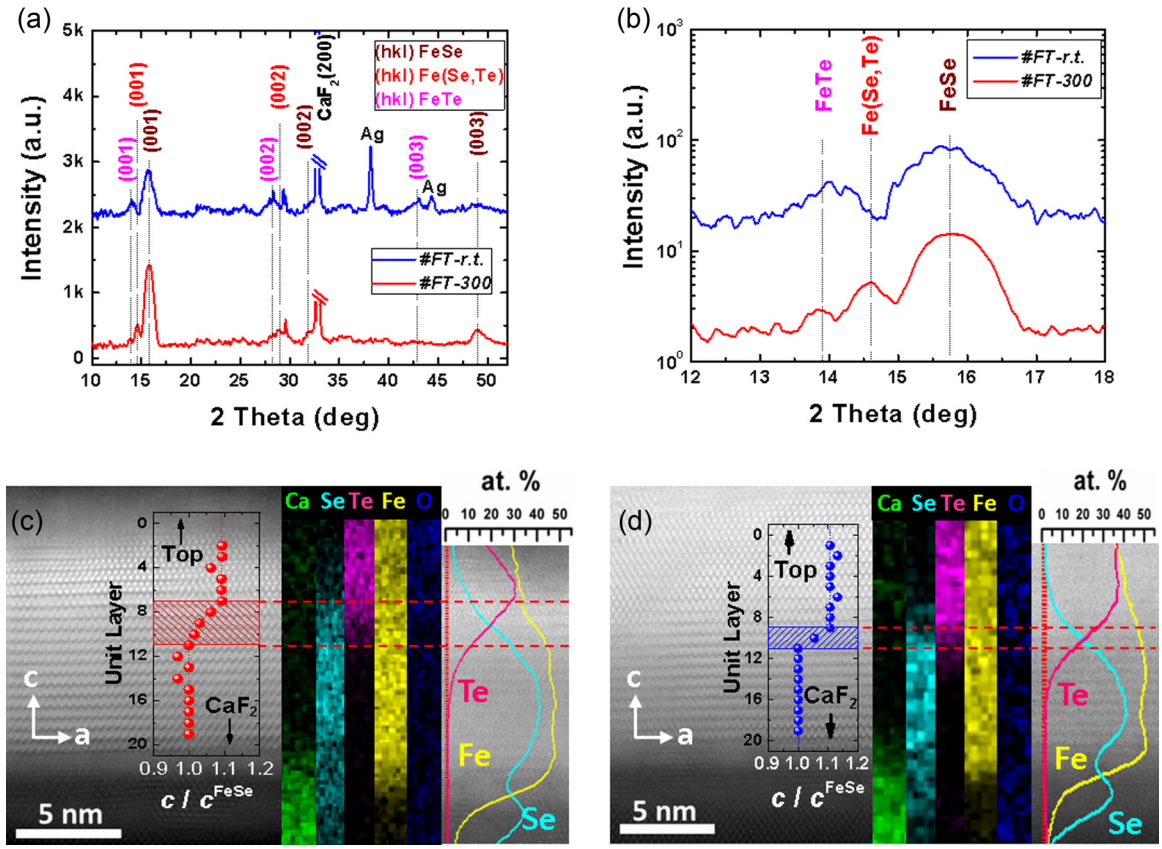

FIG. 3. (a) XRD patterns for #FT-300 (red) and #FT-r.t. (blue) in the range $2\theta = 10$–55°. The indices (hkl) represent the reflections of the FeSe (brown), Fe(Se,Te) (red), and FeTe (magenta) phases, respectively. The Ag phase in #FT-r.t. comes from the residual silver paste after transport measurements. Dashed lines are guides for the eye to mark the locations of the Fe-Chalcogenide peaks. (b) Enlarged 2θ interval near the β-FeSe (001) peak. The y axis is set to a logarithmic scale. The locations of the peaks are marked by dashed lines. The Fe(Se,Te) phase is found coexisting with FeSe and FeTe in #FT-300, while it is almost absent in #FT-r.t. (c),(d) Dark-field high-resolution STEM micrographs focusing on the FeTe/FeSe transition region from a cross-sectional viewpoint for (c) #FT-300 and (d) #FT-r.t. The two micrographs are exactly identical in scale after normalization. The corresponding EDS-mapping results are shown on the right side of each STEM image, showing the distribution of Ca (green), Se (cyan), Te (magenta), Fe (yellow), and O (blue) elements. The EDS line scans of the same region show the relative variation of Fe, Se, and Te elements in the form of atomic ratio percentages. For reference only, the relative variation trend of the c-axis lattice parameter of each Fe-chalcogenide layer was measured and is plotted on the micrograph in the form of c/c^{FeSe} vs atomic layer (c^{FeSe} refers to the c-axis lattice parameter of the first FeSe layer adjacent to the CaSe interlayer). A much broader Fe(Se,Te) diffusion layer is found in #FT-300. Red dashed lines are only guides for the eye.

which is consistent with the smaller RRR of #FT-r.t. However, considering that most of the defects are present beyond the Fe(Se,Te) region rather than inside of it, the disorder effect only affects the electrical transport properties (reflected by RRR) without influencing the superconductivity originated from the Fe(Se,Te) region. On the right side of the HAADF-STEM images, EDS analysis generated in the same area illustrates the distribution of the major elements in the films, including Ca, Se, Te, Fe, and O. The EDS results help to demonstrate the configuration of the different layers and illustrate the elemental interdiffusion. Much more Se diffuses into the upper FeTe film in #FT-300 compared with the case of #FT-r.t., due to higher evaporation rate at 300 °C, as shown more evidently by the EDS line scans. The atomic percentage (at. %) ratio of Fe remains almost stable and starts to decrease in the middle of the FeTe layer due to oxidation, while in the case of Se, the two Se-rich regions refer to the CaSe [55] interlayer (lower) and the FeSe layer (upper), respectively. Clearly, the diffusion of Se in #FT-300 even extended into the middle of the FeTe layer, leading to a much broader Fe(Se,Te) transition region compared with the much sharper FeTe/FeSe interface in #FT-r.t. In addition, O and Fe are detected in the top few nanometers of both samples without Se or Te elements, which hints at the probable existence of an Fe-oxide (FeO_x) layer above FeTe (not shown here). Similar oxidized Fe layers were also reported by Kouno *et al.* [60] in their $Fe(Se_{0.8}Te_{0.2})/CaF_2$ thin films.

In order to quantitatively investigate the layout of the Fe(Se,Te) diffusion layer at the FeSe/FeTe interface, the lattice parameters of each atomic layer were calculated from the HAADF-STEM images. To minimize error, the relative trend in the variation of the c-axis lattice parameter is defined as c/c^{FeSe}, where c and c^{FeSe} refer to the c-axis lattice parameter of the particular atomic layer and the first FeSe atomic layer adjacent to the CaSe interlayer, respectively. The atomic-layer dependence of the relative c-axis lattice parameter is plotted

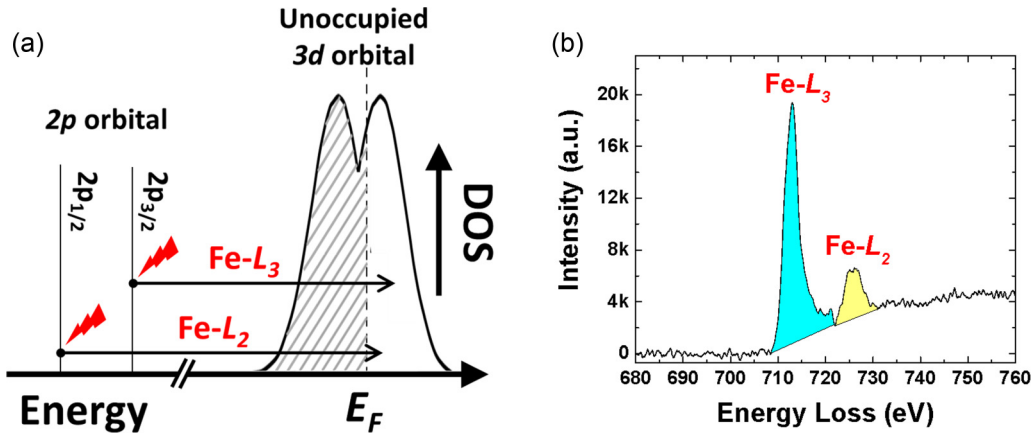

FIG. 4. (a) Schematic diagram of the electronic excitation process shows how the Fe-L_3 and Fe-L_2 edges appear in EELS. (b) An example of the Fe-L_3 (cyan) and Fe-L_2 (yellow) edges. The shaded areas are the integrals of L_3 and L_2 white lines.

in the insets of Figs. 3(c) and 3(d), ranging from the first FeSe atomic layer to the upper FeTe layers. Typical two-stage heterostructures with the same c-axis lattice parameters for the FeSe and FeTe layers are clearly exhibited in both specimens. The only difference is in the transition span of the Fe(Se,Te) diffusion layer which could be simply estimated by counting the number of atomic layers. #FT-300 has a diffusion layer about 3 unit cells in thickness, while in the case of #FT-r.t., the transition is much sharper ($\sim$1 unit cell). This is in good agreement with the XRD results, where the diffraction peak indexed as Fe(Se,Te) is only visible in #FT-300 but absent in #FT-r.t.

So far, we have proposed enhanced superconductivity in an FeTe/FeSe heterostructure with an Fe(Se,Te) diffusion layer forming near the FeTe/FeSe interface. Considering the original nonsuperconducting property of FeTe and ultrathin FeSe grown on CaF_2, a unique property from the additional Fe(Se,Te) interlayer is expected, especially for the case of #FT-300. How does a 3-unit-cell Fe(Se,Te) diffusion layer generate a T_c comparable to those of regular Fe-Se-Te films [75] with a thickness of at least one order of magnitude higher? Here, atomic-resolution EELS analysis is utilized to clarify the local electronic orbital behavior of Fe ions in FeSe, FeTe, Fe(Se,Te), etc. It is now clear that the electron filling of the Fe 3d orbital plays a critical role in determining the electronic environment on the Fermi level and the local magnetic moment in Fe-related materials [76] such as Fe metal [77,78], Fe oxides [79,80], and Fe-based superconductors [81–84]. The 3d-state occupancy can be quantitatively characterized [80] by analyzing "white-line" features in EELS spectra. In the case of Fe, the major core-loss white lines are the Fe-L_3 and Fe-L_2 edges generated due to the excitations from the Fe $2p_{3/2}$ and Fe $2p_{1/2}$ core level to unoccupied Fe 3d states [shown in Fig. 4(a)]. One typical example of Fe-$L_{3,2}$ white lines from this work is illustrated in Fig. 4(b), showing two intense edges located at the onsets near 708 and 721 eV. The method of picking an integrated area of Fe-L_3 and Fe-L_2 is based on the model proposed by Graetz *et al.* [80]. Both low-loss and core-loss spectra were collected to carry out Fourier ratio deconvolution [85] to remove the plural scattering effect. The reliability of the analysis was reflected by the value of t/λ (the quotient of the sample thickness t and the local inelastic mean free path λ) that can be calculated from the low-loss EELS spectra. The t/λ was found to range from 0.34 to 0.53 for #FT-300 and from 0.46 to 0.71 for #FT-r.t., respectively. The obtained t/λ values remained less than 1, indicating good reliability of the EELS analysis in this work.

Figure 5 shows the core-loss EELS analyses for the two samples in this work. The spectra were extracted from the dashed rectangular area shown in Fig. 5(a). Based on the data analysis method shown in Fig. 4(b), the white-line ratio Fe-L_3/L_2 as a function of position in the sample is plotted in the inset of Fig. 5(a). Overall, the trend in the position-dependent Fe-L_3/L_2 in #FT-300 and #FT-r.t. is mostly identical, with an L_3/L_2 value of $\sim$3.5 in the first 6 nm close to the CaF_2 substrate, followed by a few nanometers with a low L_3/L_2 value of $\sim$3.2, and finally boosted up to $L_3/L_2 \approx 4.9$ in the top region. The highest Fe-L_3/L_2 value of $\sim$4.9 found in the top layer in this work is correlated with the fact that the Fe ions in Fe oxides are usually in a high-spin state and have a quite large local magnetic moment [86]. This high L_3/L_2 ratio value corresponds well with a variety of EELS analyses on iron-oxygen systems done by Leapman *et al.* [87], Colliex *et al.* [88], and Chen *et al.* [79]. It evidences the existence of an FeO_x layer which arises from the degradation of the FeTe surface. As a result, the actual thickness of the FeTe layer must be lower than the nominal 7 nm, which is proved by a thin layer which spans $\sim$3 nm with the lowest L_3/L_2 value of $\sim$3.2 below the FeO_x layer. On the contrary, the FeSe layer with an L_3/L_2 value of $\sim$3.5 is thicker ($\sim$ 7 nm) because of the effective protection provided by the upper FeTe layer. The phenomenon that the FeTe layer shows a lower L_3/L_2 value than the FeSe layer resembles the results of EELS studies on inhomogeneous $Fe_{1+y}Te_xSe_{1-x}$ single crystals done by Hu *et al.* [82], where a higher/lower L_3/L_2 intensity ratio reflects the Te-poor/Te-rich region, respectively. Intriguingly, a distinct difference in L_3/L_2 between the two samples is observed in a several-unit-cells-thick region lying between the FeTe and FeSe layers. A relatively high Fe-L_3/L_2 ratio of $\sim$4.0 is found in #FT-300, while that of #FT-r.t. shows no big variation in the same region. In consideration of the principle of white-line excitation, the abnormal L_3/L_2 behavior in the FeTe/FeSe interfacial region of #FT-300 might suggest particular properties related to the electronic orbital status and will

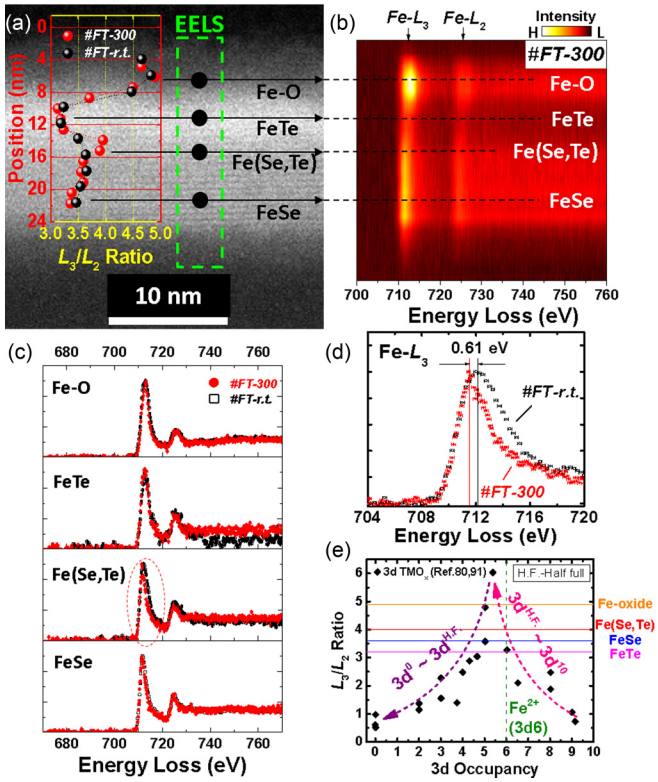

FIG. 5. Core-loss EELS results acquired at room temperature for the two samples in this work. (a) A HAADF image of #FT-300 with a dashed rectangle indicating the area where spectra were collected. The HAADF image of #FT-r.t. was taken under the same conditions (not shown here). The inset shows the position-dependent Fe-L_3/L_2 ratio in #FT-300 (red circles) and #FT-r.t. (black squares) along the EELS scan direction. A relatively high Fe-L_3/L_2 ratio in #FT-300 in the Fe(Se,Te) region is the only difference. The regions denoted as Fe-O, FeTe, Fe(Se,Te), and FeSe layers are defined based on the EDS results on #FT-300. The same definition is utilized in #FT-r.t. despite the much sharper transition. The typical areas of different regions are indicated by horizontal lines on the HAADF image as well as in the core-loss EELS mapping shown in (b). (c) Separate EELS spectra for the four regions in the two samples (red circles: #FT-300; black squares: #FT-r.t.). A dashed oval in the region of Fe(Se,Te) highlights the only difference in a white-line feature. (d) A magnified range of the EELS spectra showing the energy shift of the Fe-L_3 edge in the Fe(Se,Te) region of #FT-300 compared with that of #FT-r.t. from the same area. The error bar is 0.15 eV. (e) White-line Fe-L_3/L_2 ratios for the four regions in #FT-300 are presented in the form of horizontal lines. The "L_3/L_2 ratio–3d occupancy" results from Graetz *et al.* [80] and Sparrow *et al.* [91] are reproduced as solid diamonds for reference. The dashed arrows are a guide for the eye to show the empirical correlation between the white-line ratio and the 3d occupancy of transition-metal oxides (TMO$_x$) that was summarized in Ref. [80].

be discussed soon. Figure 5(b) presents the core-loss EELS mapping of #FT-300, with the z axis and y axis referring to the white-line edge intensity and position, respectively. The horizontal lines indicate the typical positions of four different regions (FeO$_x$, FeTe, Fe(Se,Te), and FeSe). The Fe-L_3 edge in the FeO$_x$ region is distinctly higher in energy than in the other regions. Taftø *et al.* [89] verified the determination of Fe^{2+} and Fe^{3+} ions in a mixed-valence spinel by the EELS technique and demonstrated that Fe^{3+} ions lead to higher Fe-L_3 energy than Fe^{2+} ions. Also, van Aken and Liebscher [90] reported that their Fe-L_3 edge of Fe^{3+} was 1.7 eV higher than that of Fe^{2+}. Hence, it is reasonable here for the FeO$_x$ region to show higher energy loss in the Fe-L_3 edge, as it is the only place in our samples that could possibly possess Fe^{3+} ions.

The corresponding EELS spectra taken at four indicated positions are plotted in Fig. 5(c), with each pair of spectra (#FT-300 in red circles and #FT-r.t. in black squares) compared in a separate image. Obviously, the FeO$_x$ and FeSe regions in the two samples show exactly the same white-line behavior, with the two sets of spectra overlapping with each other. In the case of the FeTe region, the tail part, generally called the "continuum background," with energy loss higher than the Fe-L_2 edge of #FT-r.t., is somewhat lower than that of #FT-300. Several factors might vary the continuum background, such as the thickness of the region analyzed, the deconvolution process used, or the exposure time spent during acquisition, but none of them is related to the intrinsic property of the analyzed sample. As a result, the spectral difference in the continuum component of FeTe spectra is considered irrelevant to the region underneath Fe(Se,Te) as well as the corresponding superconductivity. More importantly, the white-line features (Fe-$L_{3,2}$ edges) still show identical shapes, indicating the negligible effect of different heat-treatment temperatures on FeTe layers. Among all four regions, the only difference is found in the region of the Fe(Se,Te) diffusion layer. In Fig. 5(d), an enlarged range of EELS spectra from 704 to 720 eV (Fe-L_3 edge) for the Fe(Se,Te) region in Fig. 5(c) is presented. It is clearly seen that the energy loss of Fe-L_3 is 0.61 eV lower in #FT-300 compared with that in #FT-r.t. That is to say, a redshift in the Fe-L_3 edge occurs in this region if an Fe(Se,Te) diffusion layer is formed at the FeTe/FeSe interface. Several factors might result in a redshift in the Fe-L_3 edge. Hu *et al.* [82] reported a Fe-L_3 edge shifted by 0.13 eV to lower energy in their Te-rich $FeTe_{0.7}Se_{0.3}$ specimen. In our work, it may imply slightly more Te content in the Fe(Se,Te) region in #FT-300 than in #FT-r.t., although the energy redshift in our work is much larger than in the case of Hu *et al.* [82], and thus more factors are expected to be at work. Zhao *et al.* [47] conducted high-resolution EELS analyses on their MBE-FeSe/STO thin films and observed a blueshift of the Fe-L_3 edge near the FeSe/STO interface. The energy shift was then proved to be direct evidence of electron doping in the first 1–2 UC FeSe layers from the STO substrate. Therefore, the electron-doping state of the Fe(Se,Te) diffusion layer can be excluded as a reason for the enhanced T_c in this work, as we observed a redshift instead. On the contrary, extra hole carriers are likely to be introduced by FeTe deposition [47]. Moreover, the simulation carried out in the same work indicated that 3% tensile stress at the FeSe/STO interface can also result in a slight redshift in the Fe-$L_{3,2}$ edges. Considering that FeTe has a larger lattice parameter than the FeSe beneath, it should experience compressive stress. Owing to the high growth temperature of the FeTe layer in #FT-300, the stress was effectively relieved, so that a Fe-L_3 edge at lower energy should be expected in #FT-300, which coincides with the data on hand. To sum up, the phenomenon that the Fe-L_3 edge

in #FT-300 shows a 0.61 eV shift to lower energy in the Fe(Se,Te) diffusion layer than in #FT-r.t. results from a hybrid effect, including local fluctuation of Te content, additional hole carrier doping, and/or different stress conditions.

An empirical relationship has been established in 3*d* transition-metal oxides (TMO_x), where a maximum white-line ratio Fe-L_3/L_2 is obtained when the filling of the 3*d* state is approximately half full [80,91], and deviation toward either side from half-full 3*d* occupancy will lead to a lower Fe-L_3/L_2 ratio. The results are redrawn in Fig. 5(e) with dashed arrows showing the correlation between the "L_3/L_2 ratio" and "3*d* occupancy." The Fe-L_3/L_2 ratios for the four regions ($FeO_x \approx$ 4.9, FeTe $\approx$ 3.2, Fe(Se, Te) $\approx$ 4.0, and FeSe $\approx$ 3.5) in #FT-300 are added into the results for comparison. We note that a direct L_3/L_2 ratio comparison of Fe-*Ch* with 3*d* TMO_x to obtain the information about 3*d* electron occupancy might not be quantitatively accurate due to their different electronic structures. Even so, the qualitative conclusion is still valuable for reflecting tiny fluctuations of Fe 3*d* electron occupancy in different regions, considering that O, Se, and Te all belong to the chalcogen family. According to the empirical conclusion [80] that the L_3/L_2 ratio decreases when 3*d* occupancy is between d^5 and d^{10}, the higher L_3/L_2 ratio in the Fe(Se,Te) region probably implies less electron occupancy in Fe 3*d* orbitals. A different point of view was proposed by Cantoni *et al.* [81] in regard to the effect of 3*d* orbital occupancy on iron-based superconductors. They believed that the total amount of holes in Fe 3*d* orbitals is nearly constant (~ 4) in all types of iron-based compounds, with a small fluctuation in the ratio of holes in the $j = 5/2$ and $j = 3/2$ levels ($h_{5/2}/h_{3/2}$), depending on variations in the local magnetic moment. Therefore, the abnormal 3*d* electronic orbital behavior found in the Fe(Se,Te) diffusion layer in #FT-300 hints that the status of Fe 3*d* orbital occupancy is one of the key factors determining the enhanced superconductivity in the present work.

IV. CONCLUSIONS

To summarize, the common T_c suppression in ultrathin Fe-*Ch* thin films grown on a non-STO substrate is overcome in an FeTe/FeSe bilayer heterostructure by coating an FeTe capping layer on top of the FeSe layer. The enhanced T_c^{onset} in this work is 17.6 K, which is considered mostly related to a several-unit-cells-thick Fe(Se,Te) diffusion layer near the FeTe/FeSe interface observed by phase identification. The Hall coefficient results exclude the present work from the HTS Fe-*Ch* scenarios, which are usually dominated by electron-type carriers. According to EELS analyses near the interfacial region, variation in the electronic orbital structure of different regions is revealed by white-line features. Compared with the reference sample, an energy shift of the Fe-L_3 edge is noticed in the additional Fe(Se,Te) diffusion layer, indicating a hybrid consequence of the Te-rich condition, extra hole doping, and/or less compressive strain in this region. Moreover, the Fe(Se,Te) diffusion layer exhibits a higher Fe-L_3/L_2 ratio than those of either the upper FeTe or the lower FeSe layer. Following the empirical correlation established in 3*d* transition-metal oxides, lower Fe 3*d* electron occupancy is expected in the Fe(Se,Te) region. Our nanoscale EELS analysis together with macroscopic transport and phase characterizations confirm the importance of the FeTe/FeSe interface in realizing enhanced superconductivity in regular Fe-*Ch* thin films. These results will provide constructive guidance for a unified understanding of unconventional iron-based superconductivity.

ACKNOWLEDGMENTS

This work is supported by the National Natural Science Foundation of China (Grants No. 51822404 and No. 51574178), the Science and Technology Program of Tianjin (Grant No.18YFZCGX00070), and the Natural Science Foundation of Tianjin (Grant No. 18JCYBJC17900). The authors are also grateful to the Australian Research Council (Grants No. DE140101333 and No. DP170104116). This research used equipment funded by the Australian Research Council (ARC) via a Linkage, Infrastructure, Equipment and Facilities (LIEF) grant (Grants No. LE120100104 and No. LE160100063) located at the UOW Electron Microscopy Centre. The authors want to thank Dr. Gilberto Casillas Garcia for his kind assistance with microscopy. The authors are also grateful to Dr. Tania Silver for critical reading of the manuscript.

[1] I. Božović, X. He, J. Wu, and A. T. Bollinger, Dependence of the critical temperature in overdoped copper oxides on superfluid density, Nature (London) **536**, 309 (2016).

[2] A. Mann, High-temperature superconductivity at 25: Still in suspense, Nature (London) **475**, 280 (2011).

[3] J. G. Bednorz and K. A. Müller, Possible high T_c superconductivity in the Ba−La−Cu−O system, Z. Phys. B Condens. Matter **64**, 189 (1986).

[4] Y. Kamihara, T. Watanabe, M. Hirano, and H. Hosono, Iron-based layered superconductor La[$O_{1-x}F_x$]FeAs ($x =$ 0.05–0.12) with $T_c = 26$ K, J. Am. Chem. Soc. **130**, 3296 (2008).

[5] X. H. Chen, T. Wu, G. Wu, R. H. Liu, H. Chen, and D. F. Fang, Superconductivity at 43 K in $SmFeAsO_{1-x}F_x$, Nature (London) **453**, 761 (2008).

[6] M. Rotter, M. Tegel, and D. Johrendt, Superconductivity at 38 K in the Iron Arsenide ($Ba_{1-x}K_x$)Fe_2As_2, Phys. Rev. Lett. **101**, 107006 (2008).

[7] A. S. Sefat, R. Jin, M. A. McGuire, B. C. Sales, D. J. Singh, and D. Mandrus, Superconductivity at 22 K in Co-doped $BaFe_2As_2$ Crystals, Phys. Rev. Lett. **101**, 117004 (2008).

[8] X. C. Wang, Q. Q. Liu, Y. X. Lv, W. B. Gao, L. X. Yang, R. C. Yu, F. Y. Li, and C. Q. Jin, The superconductivity at 18 K in LiFeAs system, Solid State Commun. **148**, 538 (2008).

[9] M. J. Pitcher, D. R. Parker, P. Adamson, S. J. C. Herkelrath, A. T. Boothroyd, R. M. Ibberson, M. Brunelli, and S. J. Clarke, Structure and superconductivity of LiFeAs, Chem. Commun. **0**, 5918 (2008).

[10] N. Chen, Y. Liu, Z. Ma, L. Yu, and H. Li, Improvement in structure and superconductivity of bulk $FeSe_{0.5}Te_{0.5}$

superconductors by optimizing sintering temperature, Scripta Mater. **112**, 152 (2016).

[11] F.-C. Hsu, J.-Y. Luo, K.-W. Yeh, T.-K. Chen, T.-W. Huang, P. M. Wu, Y.-C. Lee, Y.-L. Huang, Y.-Y. Chu, D.-C. Yan, and M.-K. Wu, Superconductivity in the PbO-type structure alpha-FeSe, Proc. Natl. Acad. Sci. USA **105**, 14262 (2008).

[12] T. M. McQueen, Q. Huang, V. Ksenofontov, C. Felser, Q. Xu, H. Zandbergen, Y. S. Hor, J. Allred, A. J. Williams, D. Qu, J. Checkelsky, N. P. Ong, and R. J. Cava, Extreme sensitivity of superconductivity to stoichiometry in $Fe_{1+\delta}Se$, Phys. Rev. B **79**, 014522 (2009).

[13] Y. Mizuguchi, F. Tomioka, S. Tsuda, T. Yamaguchi, and Y. Takano, Superconductivity at 27K in tetragonal FeSe under high pressure, Appl. Phys. Lett. **93**, 152505 (2008).

[14] S. Margadonna, Y. Takabayashi, Y. Ohishi, Y. Mizuguchi, Y. Takano, T. Kagayama, T. Nakagawa, M. Takata, and K. Prassides, Pressure evolution of the low-temperature crystal structure and bonding of the superconductor FeSe ($T_c = 37$ K), Phys. Rev. B **80**, 064506 (2009).

[15] S. Medvedev, T. M. McQueen, I. A. Troyan, T. Palasyuk, M. I. Eremets, R. J. Cava, S. Naghavi, F. Casper, V. Ksenofontov, G. Wortmann, and C. Felser, Electronic and magnetic phase diagram of beta-$Fe_{1.01}Se$ with superconductivity at 36.7 K under pressure, Nat. Mater. **8**, 630 (2009).

[16] J. N. Millican, D. Phelan, E. L. Thomas, J. B. Leão, and E. Carpenter, Pressure-induced effects on the structure of the FeSe superconductor, Solid State Commun. **149**, 707 (2009).

[17] M. Bendele, A. Ichsanow, Y. Pashkevich, L. Keller, T. Strässle, A. Gusev, E. Pomjakushina, K. Conder, R. Khasanov, and H. Keller, Coexistence of superconductivity and magnetism in $FeSe_{1-x}$ under pressure, Phys. Rev. B **85**, 064517 (2012).

[18] K.-W. Yeh, T.-W. Huang, Y.-l. Huang, T.-K. Chen, F.-C. Hsu, P. M. Wu, Y.-C. Lee, Y.-Y. Chu, C.-L. Chen, J.-Y. Luo, D.-C. Yan, and M.-K. Wu, Tellurium substitution effect on superconductivity of the α-phase iron selenide, Europhys. Lett. **84**, 37002 (2008).

[19] T. J. Liu, J. Hu, B. Qian, D. Fobes, Z. Q. Mao, W. Bao, M. Reehuis, S. A. Kimber, K. Prokes, S. Matas, D. N. Argyriou, A. Hiess, A. Rotaru, H. Pham, L. Spinu, Y. Qiu, V. Thampy, A. T. Savici, J. A. Rodriguez, and C. Broholm, From (pi,0) magnetic order to superconductivity with (pi,pi) magnetic resonance in $Fe_{1.02}Te_{1-x}Se_x$, Nat. Mater. **9**, 718 (2010).

[20] N. Chen, Y. Liu, Z. Ma, H. Li, and M. Shahriar Al Hossain, Enhancement of superconductivity in the sintered $FeSe_{0.5}Te_{0.5}$ bulks with proper amount of Sn addition, J. Alloys Compd. **633**, 233 (2015).

[21] S. A. Moore, J. L. Curtis, C. Di Giorgio, E. Lechner, M. Abdel-Hafiez, O. S. Volkova, A. N. Vasiliev, D. A. Chareev, G. Karapetrov, and M. Iavarone, Evolution of the superconducting properties in $FeSe_{1-x}S_x$, Phys. Rev. B **92**, 235113 (2015).

[22] J. Guo, S. Jin, G. Wang, S. Wang, K. Zhu, T. Zhou, M. He, and X. Chen, Superconductivity in the iron selenide $K_xFe_2Se_2$ ($0 \leqslant x \leqslant 1.0$), Phys. Rev. B **82**, 180520 (2010).

[23] A. F. Wang, J. J. Ying, Y. J. Yan, R. H. Liu, X. G. Luo, Z. Y. Li, X. F. Wang, M. Zhang, G. J. Ye, P. Cheng, Z. J. Xiang, and X. H. Chen, Superconductivity at 32 K in single-crystalline $Rb_xFe_{2-y}Se_2$, Phys. Rev. B **83**, 060512 (2011).

[24] D. Telesca, Y. Nie, J. I. Budnick, B. O. Wells, and B. Sinkovic, Impact of valence states on the superconductivity of iron telluride and iron selenide films with incorporated oxygen, Phys. Rev. B **85**, 214517 (2012).

[25] B. Lei, J. H. Cui, Z. J. Xiang, C. Shang, N. Z. Wang, G. J. Ye, X. G. Luo, T. Wu, Z. Sun, and X. H. Chen, Evolution of High-Temperature Superconductivity from a Low-T_c Phase Tuned by Carrier Concentration in FeSe Thin Flakes, Phys. Rev. Lett. **116**, 077002 (2016).

[26] N. Lu, P. Zhang, Q. Zhang, R. Qiao, Q. He, H.-B. Li, Y. Wang, J. Guo, D. Zhang, Z. Duan, Z. Li, M. Wang, S. Yang, M. Yan, E. Arenholz, S. Zhou, W. Yang, L. Gu, C.-W. Nan, J. Wu, Y. Tokura, and P. Yu, Electric-field control of tri-state phase transformation with a selective dual-ion switch, Nature (London) **546**, 124 (2017).

[27] Y. Cui, G. Zhang, H. Li, H. Lin, X. Zhu, H.-H. Wen, G. Wang, J. Sun, M. Ma, Y. Li, D. Gong, T. Xie, Y. Gu, S. Li, H. Luo, P. Yu, and W. Yu, Protonation induced high-T_c phases in iron-based superconductors evidenced by NMR and magnetization measurements, Sci. Bull **63**, 11 (2017).

[28] Q. Wang, Z. Li, W. Zhang, Z. Zhang, J. Zhang, W. Li, H. Ding, Y. Ou, P. Deng, K. Chang, J. Wen, C. Song, K. He, J. Jia, S. Ji, Y. Wang, L. Wang, X. Chen, X. Ma, and Q.-K. Xue, Interface-induced high-temperature superconductivity in single unit-cell FeSe films on $SrTiO_3$, Chin. Phys. Lett. **29**, 037402 (2012).

[29] W. Zhang, Y. Sun, J. Zhang, F. Li, M. Guo, Y. Zhao, H. Zhang, J. Peng, Y. Xing, H. Wang, T. Fujita, A. Hirata, Z. Li, H. Ding, C. Tang, M. Wang, Q. Wang, K. He, S. Ji, X. Chen, J. Wang, Z. Xia, L. Li, Y. Wang, J. Wang, L. Wang, M. Chen, Q.-K. Xue, and X. Ma, Direct observation of high-temperature superconductivity in one-unit-cell FeSe films, Chin. Phys. Lett. **31**, 017401 (2014).

[30] W. Zhang, Z. Li, F. Li, H. Zhang, J. Peng, C. Tang, Q. Wang, K. He, X. Chen, L. Wang, X. Ma, and Q.-K. Xue, Interface charge doping effects on superconductivity of single-unit-cell FeSe films on $SrTiO_3$ substrates, Phys. Rev. B **89**, 060506(R) (2014).

[31] R. Peng, X. P. Shen, X. Xie, H. C. Xu, S. Y. Tan, M. Xia, T. Zhang, H. Y. Cao, X. G. Gong, J. P. Hu, B. P. Xie, and D. L. Feng, Measurement of an Enhanced Superconducting Phase and a Pronounced Anisotropy of the Energy Gap of a Strained FeSe Single Layer in FeSe/Nb: $SrTiO_3/KTaO_3$ Heterostructures Using Photoemission Spectroscopy, Phys. Rev. Lett. **112**, 107001 (2014).

[32] S. He, J. He, W. Zhang, L. Zhao, D. Liu, X. Liu, D. Mou, Y.-B. Ou, Q.-Y. Wang, Z. Li, L. Wang, Y. Peng, Y. Liu, C. Chen, L. Yu, G. Liu, X. Dong, J. Zhang, C. Chen, Z. Xu, X. Chen, X. Ma, Q. Xue, and X. J. Zhou, Phase diagram and electronic indication of high-temperature superconductivity at 65 K in single-layer FeSe films, Nat. Mater. **12**, 605 (2013).

[33] D. Liu, W. Zhang, D. Mou, J. He, Y.-B. Ou, Q.-Y. Wang, Z. Li, L. Wang, L. Zhao, S. He, Y. Peng, X. Liu, C. Chen, L. Yu, G. Liu, X. Dong, J. Zhang, C. Chen, Z. Xu, J. Hu, X. Chen, X. Ma, Q. Xue, and X. J. Zhou, Electronic origin of high-temperature superconductivity in single-layer FeSe superconductor, Nat. Commun. **3**, 931 (2012).

[34] S. Tan, Y. Zhang, M. Xia, Z. Ye, F. Chen, X. Xie, R. Peng, D. Xu, Q. Fan, H. Xu, J. Jiang, T. Zhang, X. Lai, T. Xiang, J. Hu, B. Xie, and D. Feng, Interface-induced superconductivity and strain-dependent spin density waves in $FeSe/SrTiO_3$ Thin Films, Nat. Mater. **12**, 634 (2013).

[35] Y. T. Cui, R. G. Moore, A. M. Zhang, Y. Tian, J. J. Lee, F. T. Schmitt, W. H. Zhang, W. Li, M. Yi, Z. K. Liu, M. Hashimoto, Y. Zhang, D. H. Lu, T. P. Devereaux, L. L. Wang, X. C. Ma, Q. M. Zhang, Q. K. Xue, D. H. Lee, and Z. X. Shen, Interface Ferroelectric Transition near the Gap-Opening Temperature in a Single-Unit-Cell FeSe Film Grown on Nb-Doped $SrTiO_3$ Substrate, Phys. Rev. Lett. **114**, 037002 (2015).

[36] J. Ge, Z. Liu, C. Liu, C. Gao, D. Qian, Q.-K. Xue, Y. Liu, and J. Jia, Superconductivity above 100 K in single-layer FeSe films on doped $SrTiO_3$, Nat. Mater. **14**, 285 (2015).

[37] Z. F. Wang, H. Zhang, D. Liu, C. Liu, C. Tang, C. Song, Y. Zhong, J. Peng, F. Li, C. Nie, L. Wang, X. J. Zhou, X. Ma, Q. K. Xue, and F. Liu, Topological edge states in a high-temperature superconductor FeSe/$SrTiO_3$(001) film, Nat. Mater. **15**, 968 (2016).

[38] G. N. Phan, K. Nakayama, S. Kanayama, M. Kuno, K. Sugawara, T. Sato, and T. Takahashi, High-temperature superconductivity and lattice relaxation in lithium-deposited FeSe on $SrTiO_3$, J. Phys. Soc. Jpn. **86**, 033706 (2017).

[39] C. Tang, C. Liu, G. Zhou, F. Li, H. Ding, Z. Li, D. Zhang, Z. Li, C. Song, S. Ji, K. He, L. Wang, X. Ma, and Q.-K. Xue, Interface-enhanced electron-phonon coupling and high-temperature superconductivity in potassium-coated ultrathin FeSe films on $SrTiO_3$, Phys. Rev. B **93**, 020507 (2016).

[40] C. Song, H. Zhang, Y. Zhong, X. Hu, S. Ji, L. Wang, K. He, X. Ma, and Q.-K. Xue, Observation of Double-Dome Superconductivity in Potassium-Doped FeSe Thin Films, Phys. Rev. Lett. **116**, 157001 (2016).

[41] Y. Miyata, K. Nakayama, K. Sugawara, T. Sato, and T. Takahashi, High-temperature superconductivity in potassium-coated multilayer FeSe thin films, Nat. Mater. **14**, 775 (2015).

[42] C. Tang, D. Zhang, Y. Zang, C. Liu, G. Zhou, Z. Li, C. Zheng, X. Hu, C. Song, S. Ji, K. He, X. Chen, L. Wang, X. Ma, and Q.-K. Xue, Superconductivity dichotomy in K-coated single and double unit cell FeSe films on $SrTiO_3$, Phys. Rev. B **92**, 180507 (2015).

[43] W. H. Zhang, X. Liu, C. H. P. Wen, R. Peng, S. Y. Tan, B. P. Xie, T. Zhang, and D. L. Feng, Effects of surface electron doping and substrate on the superconductivity of epitaxial FeSe films, Nano Lett. **16**, 1969 (2016).

[44] Q. Y. Wang, W. H. Zhang, Z. C. Zhang, Y. Sun, Y. Xing, Y. Y. Wang, L. L. Wang, X. C. Ma, Q. K. Xue, and J. Wang, Thickness dependence of superconductivity and superconductor–insulator transition in ultrathin FeSe films on $SrTiO_3$ (001) substrate, 2D Mater. **2**, 044012 (2015).

[45] J. Shiogai, Y. Ito, T. Mitsuhashi, T. Nojima, and A. Tsukazaki, Electric-field-induced superconductivity in electrochemically etched ultrathin FeSe films on $SrTiO_3$ and MgO, Nat. Phys. **12**, 42 (2016).

[46] J. Shiogai, T. Miyakawa, Y. Ito, T. Nojima, and A. Tsukazaki, Unified trend of superconducting transition temperature versus Hall coefficient for ultrathin FeSe films prepared on different oxide substrates, Phys. Rev. B **95**, 115101 (2017).

[47] W. Zhao, M. Li, C.-Z. Chang, J. Jiang, L. Wu, C. Liu, J. S. Moodera, Y. Zhu, and M. H. W. Chan, Direct imaging of electron transfer and its influence on superconducting pairing at FeSe/$SrTiO_3$ interface, Sci. Adv. **4**, eaao2682 (2018).

[48] W. Si, Z.-W. Lin, Q. Jie, W.-G. Yin, J. Zhou, G. Gu, P. D. Johnson, and Q. Li, Enhanced superconducting transition temperature in $FeSe_{0.5}Te_{0.5}$ thin films, Appl. Phys. Lett. **95**, 052504 (2009).

[49] P. Yuan, Z. Xu, Y. Ma, Y. Sun, and T. Tamegai, Optimization of deposition conditions to grow high-quality Fe-Se-Te thin films, IEEE Trans. Appl. Supercond. **27**, 1 (2017).

[50] Y. Imai, T. Akiike, M. Hanawa, I. Tsukada, A. Ichinose, A. Maeda, T. Hikage, T. Kawaguchi, and H. Ikuta, Systematic comparison of eight substrates in the growth of $FeSe_{0.5}Te_{0.5}$ superconducting thin films, Appl. Phys. Express **3**, 043102 (2010).

[51] P. Mele, K. Matsumoto, K. Fujita, Y. Yoshida, T. Kiss, A. Ichinose, and M. Mukaida, Fe-Te-Se epitaxial thin films with enhanced superconducting properties, Supercond. Sci. Technol. **25**, 084021 (2012).

[52] F. Nabeshima, Y. Imai, A. Ichinose, I. Tsukada, and A. Maeda, Growth and transport properties of FeSe/FeTe superlattice thin films, Jpn. J. Appl. Phys. **56**, 020308 (2017).

[53] F. Nabeshima, Y. Imai, M. Hanawa, I. Tsukada, and A. Maeda, Enhancement of the superconducting transition temperature in FeSe epitaxial thin films by anisotropic compression, Appl. Phys. Lett. **103**, 172602 (2013).

[54] I. Tsukada, A. Ichinose, F. Nabeshima, Y. Imai, and A. Maeda, Origin of lattice compression of $FeSe_{1-x}Te_x$ thin films on CaF_2 substrates, AIP Adv. **6**, 095314 (2016).

[55] W. Qiu, Z. Ma, D. Patel, L. Sang, C. Cai, M. Shahriar Al Hossain, Z. Cheng, X. Wang, and S. X. Dou, The interface structure of FeSe thin film on CaF_2 substrate and its influence on the superconducting performance, ACS Appl. Mater. Interfaces **9**, 37446 (2017).

[56] E. Bellingeri, I. Pallecchi, R. Buzio, A. Gerbi, D. Marrè, M. R. Cimberle, M. Tropeano, M. Putti, A. Palenzona, and C. Ferdeghini, $T_c = 21$ K in epitaxial $FeSe_{0.5}Te_{0.5}$ thin films with biaxial compressive strain, Appl. Phys. Lett. **96**, 102512 (2010).

[57] M. J. Wang, J. Y. Luo, T. W. Huang, H. H. Chang, T. K. Chen, F. C. Hsu, C. T. Wu, P. M. Wu, A. M. Chang, and M. K. Wu, Crystal Orientation and Thickness Dependence of the Superconducting Transition Temperature of Tetragonal $FeSe_{1-x}$ Thin Films, Phys. Rev. Lett. **103**, 117002 (2009).

[58] A. Tsukada, K. E. Luna, R. H. Hammond, M. R. Beasley, J. F. Zhao, and S. H. Risbud, Pulsed laser deposition conditions and superconductivity of FeSe thin films, Appl. Phys. A **104**, 311 (2011).

[59] Y. F. Nie, E. Brahimi, J. I. Budnick, W. A. Hines, M. Jain, and B. O. Wells, Suppression of superconductivity in FeSe films under tensile strain, Appl. Phys. Lett. **94**, 242505 (2009).

[60] S. Kouno, Y. Sato, Y. Katayama, A. Ichinose, D. Asami, F. Nabeshima, Y. Imai, A. Maeda, and K. Ueno, Superconductivity at 38 K in an electrochemical interface between ionic liquid and $Fe(Se_{0.8}Te_{0.2})$ on various substrates, arXiv:1805.02380.

[61] R. Schneider, A. G. Zaitsev, D. Fuchs, and H. v. Löhneysen, Superconductor-Insulator Quantum Phase Transition in Disordered FeSe Thin Films, Phys. Rev. Lett. **108**, 257003 (2012).

[62] W. Si, Q. Jie, L. Wu, J. Zhou, G. Gu, P. D. Johnson, and Q. Li, Superconductivity in epitaxial thin films of $Fe_{1.08}Te : O_x$, Phys. Rev. B **81**, 092506 (2010).

[63] Y. F. Nie, D. Telesca, J. I. Budnick, B. Sinkovic, and B. O. Wells, Superconductivity induced in iron telluride films by low-temperature oxygen incorporation, Phys. Rev. B **82**, 020508 (2010).

[64] G. Zhou, D. Zhang, C. Liu, C. Tang, X. Wang, Z. Li, C. Song, S. Ji, K. He, L. Wang, X. Ma, and Q.-K. Xue, Interface induced high temperature superconductivity in single unit-cell FeSe on $SrTiO_3$(110), Appl. Phys. Lett. **108**, 202603 (2016).

[65] Y. Sun, W. Zhang, Y. Xing, F. Li, Y. Zhao, Z. Xia, L. Wang, X. Ma, Q. K. Xue, and J. Wang, High temperature superconducting FeSe films on $SrTiO_3$ substrates, Sci. Rep. **4**, 6040 (2014).

[66] B. Lei, Z. J. Xiang, X. F. Lu, N. Z. Wang, J. R. Chang, C. Shang, A. M. Zhang, Q. M. Zhang, X. G. Luo, T. Wu, Z. Sun, and X. H. Chen, Gate-tuned superconductor-insulator transition in (Li,Fe)OHFeSe, Phys. Rev. B **93**, 060501 (2016).

[67] A. Maeda, F. Nabeshima, H. Takahashi, T. Okada, Y. Imai, I. Tsukada, M. Hanawa, S. Komiya, and A. Ichinose, Synthesis, characterization, Hall effect and THz conductivity of epitaxial thin films of Fe chalcogenide superconductors, Appl. Surf. Sci. **312**, 43 (2014).

[68] F. Rullier-Albenque, D. Colson, A. Forget, P. Thuéry, and S. Poissonnet, Hole and electron contributions to the transport properties of $Ba(Fe_{1-x}Ru_x)_2As_2$ single crystals, Phys. Rev. B **81**, 224503 (2010).

[69] F. Rullier-Albenque, D. Colson, A. Forget, and H. Alloul, Hall Effect and Resistivity Study of the Magnetic Transition, Carrier Content, and Fermi-Liquid Behavior in $Ba(Fe_{1-x}Co_x)_2As_2$, Phys. Rev. Lett. **103**, 057001 (2009).

[70] T. Terashima, N. Kikugawa, S. Kasahara, T. Watashige, Y. Matsuda, T. Shibauchi, and S. Uji, Magnetotransport study of the pressure-induced antiferromagnetic phase in FeSe, Phys. Rev. B **93**, 180503 (2016).

[71] K. K. Huynh, Y. Tanabe, T. Urata, H. Oguro, S. Heguri, K. Watanabe, and K. Tanigaki, Electric transport of a single-crystal iron chalcogenide FeSe superconductor: Evidence of symmetry-breakdown nematicity and additional ultrafast Dirac cone-like carriers, Phys. Rev. B **90**, 144516 (2014).

[72] Y. Sun, S. Pyon, and T. Tamegai, Electron carriers with possible Dirac-cone-like dispersion in $FeSe_{1-x}S_x$ ($x = 0$ and 0.14) single crystals triggered by structural transition, Phys. Rev. B **93**, 104502 (2016).

[73] B. Shen, Z.-P. Feng, J.-W. Huang, Y. Hu, Q. Gao, C. Li, X. Yu, G.-D. Liu, L. Yu, L. Zhao, K. Jin, and X. J. Zhou, Electronic structure and nematic phase transition in superconducting multiple-layer FeSe films grown by pulsed laser deposition method, Chin. Phys. B **26**, 077402 (2017).

[74] Y. Mizuguchi, F. Tomioka, S. Tsuda, T. Yamaguchi, and Y. Takano, FeTe as a candidate material for new iron-based superconductor, Physica C **469**, 1027 (2009).

[75] J. C. Zhuang, W. K. Yeoh, X. Y. Cui, J. H. Kim, D. Q. Shi, Z. X. Shi, S. P. Ringer, X. L. Wang, and S. X. Dou, Enhancement of transition temperature in $Fe_xSe_{0.5}Te_{0.5}$ film via iron vacancies, Appl. Phys. Lett. **104**, 262601 (2014).

[76] P. S. Miedema and F. M. F. de Groot, The iron L edges: Fe 2p X-ray absorption and electron energy loss spectroscopy, J. Electron. Spectrosc. Relat. Phenom. **187**, 32 (2013).

[77] D. H. Pearson, C. C. Ahn, and B. Fultz, White lines and d-electron occupancies for the 3d and 4d transition metals, Phys. Rev. B **47**, 8471 (1993).

[78] D. H. Pearson, B. Fultz, and C. C. Ahn, Measurements of 3*d* state occupancy in transition metals using electron energy loss spectrometry, Appl. Phys. Lett. **53**, 1405 (1988).

[79] K.-F. Chen, S.-C. Lo, L. Chang, R. Egerton, J.-J. Kai, J.-J. Lin, and F.-R. Chen, Valence state map of iron oxide thin film obtained from electron spectroscopy imaging series, Micron **38**, 354 (2007).

[80] J. Graetz, C. C. Ahn, H. Ouyang, P. Rez, and B. Fultz, White lines and *d*-band occupancy for the 3*d* transition-metal oxides and lithium transition-metal oxides, Phys. Rev. B **69**, 235103 (2004).

[81] C. Cantoni, J. E. Mitchell, A. F. May, M. A. McGuire, J. C. Idrobo, T. Berlijn, E. Dagotto, M. F. Chisholm, W. Zhou, S. J. Pennycook, A. S. Sefat, and B. C. Sales, Orbital occupancy and charge doping in iron-based superconductors, Adv. Mater. **26**, 6193 (2014).

[82] H. Hu, J.-M. Zuo, J. Wen, Z. Xu, Z. Lin, Q. Li, G. Gu, W. K. Park, and L. H. Greene, Phase separation in the iron chalcogenide superconductor $Fe_{1+y}Te_xSe_{1-x}$, New J. Phys. **13**, 053031 (2011).

[83] D. J. Singh, Electronic structure and doping in $BaFe_2As_2$ and LiFeAs: Density functional calculations, Phys. Rev. B **78**, 094511 (2008).

[84] A. Subedi, L. Zhang, D. J. Singh, and M. H. Du, Density functional study of FeS, FeSe, and FeTe: Electronic structure, magnetism, phonons, and superconductivity, Phys. Rev. B **78**, 134514 (2008).

[85] R. F. Egerton, *Electron Energy-Loss Spectroscopy in the Electron Microscope*, 3rd ed. (Springer, New York, 2011).

[86] F. M. F. de Groot, X-ray absorption and dichroism of transition metals and their compounds, J. Electron Spectrosc. Relat. Phenom. **67**, 529 (1994).

[87] R. D. Leapman, L. A. Grunes, and P. L. Fejes, Study of the L_{23} edges in the 3*d* transition metals and their oxides by electron-energy-loss spectroscopy with comparisons to theory, Phys. Rev. B **26**, 614 (1982).

[88] C. Colliex, T. Manoubi, and C. Ortiz, Electron-energy-loss-spectroscopy near-edge fine structures in the iron-oxygen system, Phys. Rev. B **44**, 11402 (1991).

[89] J. Taftø and O. L. Krivanek, Site-Specific Valence Determination by Electron Energy-Loss Spectroscopy, Phys. Rev. Lett. **48**, 560 (1982).

[90] P. A. van Aken and B. Liebscher, Quantification of ferrous/ferric ratios in minerals: new evaluation schemes of Fe L_{23} electron energy-loss near-edge spectra, Phys. Chem. Minerals **29**, 188 (2002).

[91] T. G. Sparrow, B. G. Williams, C. N. R. Rao, and J. M. Thomas, L_3/L_2 white-line intensity ratios in the electron energy-loss spectra of 3d transition-metal oxides, Chem. Phys. Lett. **108**, 547 (1984).